The role of Poiseuille flow in creating depth-variation of asthenospheric shear

Svetlana I. Natarov and Clinton P. Conrad

Department of Geology and Geophysics, SOEST, University of Hawai'i at Manoa, Hawaii, USA. E-mail: sport@hawaii.edu

SUMMARY

Asthenospheric flow accommodates differential shear between plate and mantle motions (Couette flow) and hosts additional flow driven by horizontal pressure gradients (Poiseuille flow) that may be associated with mantle upwelling and subduction. Large uncertainties in the upper mantle flow field and its rheological structure have thus far hindered our ability to constrain the relative importance of Couette and Poiseuille flows in the asthenosphere. However, quantifying the relative contributions of asthenospheric Couette and Poiseuille flows and determining the pattern of their distribution around the globe could help discriminate among competing theories of asthenospheric origin and shed light on thermal history of the Earth. We propose a new method to quantify asthenospheric Poiseuille flow using observations of the depth-dependence of azimuthal seismic anisotropy, which can be obtained from frequency-dependent surface wave tomography models. In particular, we employ a simple 1-D Couette-Poiseuille flow model and analytically solve for depth-profiles of the strain axis orientations, which approximates the orientations of azimuthal seismic anisotropy. We show that Couette-Poiseuille flow induces rotation of azimuthal seismic anisotropy with depth provided that the horizontal pressure gradient has a component transverse to plate motion. We then construct an algorithm that uses depth rotations of azimuthal anisotropy to invert for horizontal pressure gradients everywhere in the asthenosphere and test it on a global numerical mantle flow model. A comparison of pressure gradients predicted using our method with those computed directly from the numerical model shows that our algorithm is stable and accurate, unless the pressure gradient is nearly parallel to plate motion. Applying this method to seismic data will require additional constraints on asthenospheric geometry and viscosity structure. In the numerical model, we establish that Poiseuille flow drives ∼40 per cent of the total flow velocity amplitude in the asthenosphere, which indicates that pressure gradients from mantle convection may be an important component of asthenospheric dynamics that can, in principle, be constrained seismically.

Key words: Mantle processes; Seismic anisotropy; Dynamics of lithosphere and mantle.

1 INTRODUCTION

Recent analytical and numerical studies indicate that viscous flow in the asthenosphere (the mechanically weak, low viscosity layer below the lithosphere e.g. Conrad & Behn 2010; Karato 2012) is largely a combination of Couette and Poiseuille flows (Lenardic *et al.* 2006; Höink & Lenardic 2010; Crowley & O'Connell 2012). An idealized Couette flow (also called a shear-driven flow) involves viscous shearing between parallel flat plates of infinite dimensions, driven by a steady motion of one of the plates (e.g. Couette 1890). Poiseuille flow (also called a pressure-driven flow) occurs between parallel plates of infinite width and length and is driven by a horizontal pressure gradient Poiseuille (1840a,b,c). In the Earth's asthenosphere, Couette flow arises to accommodate dif-

ferential shear between plate motions and the convecting mantle (e.g. Richards *et al.* 2001) and, according to classical plate tectonic theory, is thought to dominate most asthenospheric regions away from plate boundaries and hotspots (e.g. Turcotte & Schubert 1967). Asthenospheric Poiseuille flow, on the other hand, may be induced by mantle upwellings and downwellings (Turcotte & Schubert 1967; Ryan 1990; Lenardic *et al.* 2006; Höink & Lenardic 2010), the motion of continental keels through the upper mantle (Ricard *et al.* 1988; Harig *et al.* 2010), and variations in asthenospheric thickness (e.g. Batchelor 1967), all of which can generate horizontal pressure gradients.

Unfortunately, determining the relative importance of Couette and Poiseuille flow components in the asthenosphere has been difficult due to large uncertainties in constraining the mantle's flow

field and rheology (e.g. Karato & Wu 1993; Savage 1999; Savage & Holt 2002). However, quantifying the Poiseuille component of asthenospheric flow and determining its spatial distribution around the globe could help answer several outstanding questions in mantle dynamics. For example, Couette and Poiseuille flows in the asthenosphere have been linked to different modes of mantle convection: Couette flow is found to correspond to the active lid regime of mantle convection while Poiseuille flow dominates for the sluggish lid mode (Solomatov 1995; Höink & Lenardic 2010) and is important for intermediate modes (Crowley & O'Connell 2012). Because the efficiency of planetary cooling depends on the convective mode (Solomatov 1995; Crowley & O'Connell 2012), constraining the relative importance of these two flow components may shed light on the convective regimes of present and past Earth, and, as a result, help elucidate Earth's thermal history (Korenaga 2008; Silver & Behn 2008).

Poiseuille flow may also explain specific geologic features. For example, Poiseuille flow may provide an explanation for the existence of asymmetries in subsidence rate, seamount counts, shear wave splitting delays, electrical conductivity and other geophysical observables across the East Pacific Rise (EPR) (Conder *et al.* 2002; Toomey *et al.* 2002). Specifically, eastward-directed Poiseuille flow is believed to experience a component of upwelling beneath the western flank of the EPR, where it encounters increasingly thinner lithosphere, and a component of downwelling to the east of the EPR. This, in turn, should create asymmetry in the melting region across the EPR and could explain the observed asymmetries (Conder *et al.* 2002). Asthenospheric Poiseuille flow also forms the basis of the 'plume-fed asthenosphere' hypothesis, in which the redistribution of hot material continuously supplied by mantle plumes is proposed as the source and the main driver of the asthenospheric flow (e.g. Phipps Morgan *et al.* 1995; Phipps Morgan & Smith 2002; Yamamoto *et al.* 2007). Finally, Poiseuille flow may be important for driving trench-parallel flow (Long & Silver 2009) within a thin low-viscosity layer beneath slabs (Phipps Morgan *et al.* 2007).

Couette flow shears asthenosphere, which produces lattice preferred orientation (LPO) of olivine crystals that is detectable as seismic anisotropy (e.g. McKenzie 1979; Ribe 1989; Karato & Wu 1993). Observations of seismic anisotropy have previously been attributed to a Couette flow (Gaboret *et al.* 2003; Behn *et al.* 2004; Hammond *et al.* 2005; Becker *et al.* 2006a,b; Conrad *et al.* 2007;

Conrad & Behn 2010). A pure Couette flow produces a simple shear strain rate with constant amplitude and, by itself, cannot induce seismically detectable depth variations in the orientation of the LPO (Fig. 1A). However, the amplitude of the simple shear strain rate that results from Poiseuille flow varies with depth: it is maximized at the top and at the base of the asthenosphere and is minimized in the mid-asthenosphere. Hence, when combined with Couette flow, Poiseuille flow should cause the shearing orientation, and presumably also azimuthal seismic anisotropy, to rotate with depth, provided that the pressure gradient has a component transverse to plate motion (Fig. 1B). Therefore, it should be possible to use the depth-dependence of asthenospheric azimuthal seismic anisotropy to constrain horizontal pressure gradients, and consequently, to quantify the magnitude and orientation of Poiseuille flow in the asthenosphere.

Depth profiles of the orientation of azimuthal seismic anisotropy can be obtained from frequency-dependent surface wave tomography models. Both global (e.g. Becker *et al.* 2003; Debayle *et al.* 2005; Becker *et al.* 2007) and regional (e.g. Marone & Romanowicz 2007; Hansen *et al.* 2008; Deschamps *et al.* 2008; Lin *et al.* 2010; Yuan & Romanowicz 2010) models of seismic anisotropy show significant variations in the orientation of azimuthal seismic anisotropy with depth in the asthenosphere. Several studies have attributed the observed depth-variations in azimuthal seismic anisotropy to a transition from the lithosphere, which may host several layers of fossil anisotropic fabric reflecting past deformation events, to the asthenosphere where anisotropy formation is flow-driven (e.g. Deschamps *et al.* 2008; Gao *et al.* 2010; Huang *et al.* 2011; Vinnik *et al.* 2012). Most numerical models of global mantle flow (e.g. Becker *et al.* 2003; Conrad & Behn 2010) ignore the deformation history of the lithosphere, and hence, do not predict fossil anisotropy. Nonetheless, these models predict active LPO development in the asthenosphere, and several authors (e.g. Conrad *et al.* 2007) find depth rotations about a vertical axis of azimuthal seismic anisotropy with laterally varying amplitude of up to several tens of degrees within the asthenosphere (Fig. 2). This suggests that some of the seismically observed depth-variations of anisotropy may be due to flow variations within the asthenosphere itself, instead of (or in addition to) a lithosphere–asthenosphere contrast.

Here, we develop a new method to quantify Poiseuille flow in the asthenosphere using depth-dependence of asthenospheric shear.
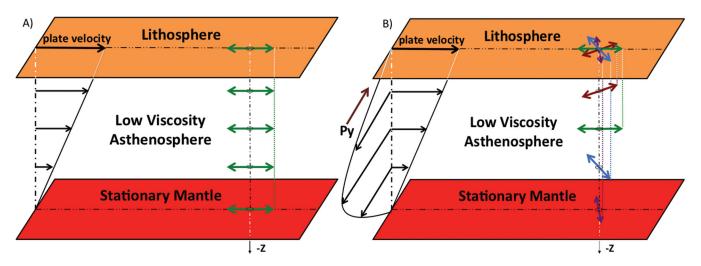

Figure 1. Dominant flow regimes in the asthenosphere (left column) and associated LPO (right column) in the reference frame of the mantle: (A) pure Couette flow does not induce changes in the orientation of LPO with depth; (B) the combination of Couette flow and Poiseuille flow perpendicular to plate motion does lead to rotation of LPO with depth.
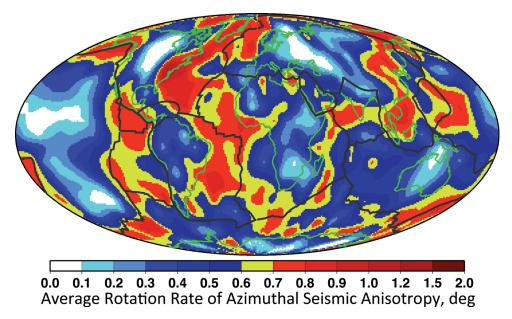
Figure 2. Average rotation of azimuthal seismic anisotropy per kilometres of asthenosphere for the GMFM (Conrad & Behn 2010). The global average value is 0.5 deg km^{-1}.

We test our method on the output of a numerical global mantle flow model (GMFM) (Conrad *et al.* 2007; Conrad & Behn 2010), which has been used to predict a variety of geophysical observables including plate motions (van Summeren *et al.* 2012), intraplate volcanism (Conrad *et al.* 2011) and SKS splitting observations (Conrad & Behn 2010). Specifically, we implement a grid search algorithm to find the horizontal pressure gradient magnitude and orientation that minimizes the misfit between depth profiles of the asthenospheric infinite strain axis (ISA) orientations computed by the GMFM and strain axis orientations derived analytically for a Couette–Poiseuille flow with constant Newtonian viscosity. The ISA is the asymptotic orientation of the long axis of the finite strain ellipsoid upon exposure to an infinite amount of constant strain, and serves as an approximation for the LPO (Kaminski & Ribe 2002). We apply our algorithm to the depth profiles of asthenospheric ISA orientations below each surface grid point of the GMFM. To test our method, we compare our results to the pressure gradients computed directly by the GMFM (Conrad & Behn 2010). We find that the pressure gradient magnitudes and directions rendered by our method closely match those computed by the GMFM. Finally, we separate the Couette and Poiseuille components of the asthenospheric flow in the GMFM and compare their relative contributions to the total flow balance in the asthenosphere.

2 ANALYTICAL COUETTE–POISEUILLE MODEL FOR A NEWTONIAN FLUID WITH CONSTANT VISCOSITY

We consider a fully developed plane Poiseuille flow with an upper plate moving with constant speed, u_o. This flow is called a plane Couette–Poiseuille flow (e.g. Papanastasiou *et al.* 2000) and is governed by the Navier-Stokes equations. Under the lubrication approximation, the horizontal pressure gradient is balanced by the vertical gradient of the shear stresses (Batchelor 1967). Hence, the Navier-Stokes equations simplify to

$$-\frac{\partial p}{\partial x_1} + \frac{\partial}{\partial x_3}\left(\mu(x_3)\frac{\partial u_1(x_3)}{\partial x_3}\right) = 0 \tag{1a}$$

$$-\frac{\partial p}{\partial x_2} + \frac{\partial}{\partial x_3}\left(\mu(x_3)\frac{\partial u_2(x_3)}{\partial x_3}\right) = 0, \tag{1b}$$

where $\frac{\partial p}{\partial x_1}$ and $\frac{\partial p}{\partial x_2}$ are horizontal pressure gradients along and orthogonal to plate motion (positive pressure is compressive), μ is viscosity (which can vary with depth), and u_1 and u_2 are velocity components along x_1 and x_2. We orient x_1 in the direction of plate motion in the reference frame of the mantle, let x_3 point up and select x_2 so that the resulting coordinate system is right-handed. We allow components of velocity in the x_1 and x_2 directions (u_1 and u_2) to vary with depth and proceed to first solve (1) for a fluid with Newtonian rheology (where stress and strain are related in a linear fashion) and constant depth-independent viscosity. For such a fluid, a dimensionless form of (1), which we use to express the trade-offs among the governing parameters, is given by

$$-\alpha_1 + \frac{\partial^2 U_1(X_3)}{\partial X_3^2} = 0 \tag{2a}$$

$$-\alpha_2 + \frac{\partial^2 U_2(X_3)}{\partial X_3^2} = 0 \tag{2b}$$

and the dimensionless set of boundary conditions is

$$U_1(0) = 1 \qquad\qquad U_1(-1) = 0 \tag{3a}$$

$$U_2(0) = 0 \qquad\qquad U_2(-1) = 0, \tag{3b}$$

where we have defined the following dimensionless quantities:

$$U = \frac{u}{u_o} \tag{4a}$$

$$X_3 = \frac{x_3}{H} \tag{4b}$$

$$\alpha_1 = \frac{H^2}{u_o\mu}\frac{\mathrm{d}p}{\mathrm{d}x_1} \tag{4c}$$

$$\alpha_2 = \frac{H^2}{u_o\mu}\frac{\mathrm{d}p}{\mathrm{d}x_2}. \tag{4d}$$

In the above, X_1, X_2 and X_3 are the dimensionless versions of x_1, x_2 and x_3, H is the layer thickness and u_o is the velocity of the top plate in the x_1 direction relative to an assumed stationary mantle. The parameters α_1 and α_2 are the dimensionless components of the pressure gradient in x_1 and x_2 directions. The magnitude, α, and the direction, θ, of the dimensionless pressure gradient are given by

$$\alpha = \sqrt{\alpha_1^2 + \alpha_2^2}, \tag{5}$$

$$\theta = \tan^{-1}\left(\frac{\alpha_2}{\alpha_1}\right). \tag{6}$$

The particular solution of (2) given (3) is

$$U_1(X_3) = \frac{1}{2}\alpha_1 X_3^2 + \left(\frac{1}{2}\alpha_1 + 1\right)X_3 + 1 \tag{7a}$$

$$U_2(X_3) = \frac{1}{2}\alpha_2 X_3^2 + \frac{1}{2}\alpha_2 X_3. \tag{7b}$$

Differentiating (7) with respect to X_3 yields

$$\frac{dU_1}{dX_3} = \alpha_1 X_3 + \frac{1}{2}\alpha_1 + 1 \tag{8a}$$

$$\frac{dU_2}{dX_3} = \alpha_2 X_3 + \frac{1}{2}\alpha_2. \tag{8b}$$

Expression (8) serves as an analytical predictor of strain axis orientation as a function of depth in the upper mantle. Exploring the behaviour of (8), we discover that pure Couette flow, (i.e. keeping $\alpha = 0$), produces shear in the direction of plate motion (i.e. $\frac{\partial U_1}{\partial X_3} = 1$, $\frac{\partial U_2}{\partial X_3} = 0$). However, introducing a dimensionless constant horizontal pressure gradient transverse to the motion of the plate, i.e. setting $\alpha_2 \neq 0$, produces rotation of the strain axis with depth (Fig. 3A). This occurs because the amplitude of simple shear generated by Poiseuille flow varies with depth while the amplitude of simple shear produced by Couette flow is depth independent. In general, a stronger transverse component of the pressure gradient results in larger rotation angles and more rapid rotation with depth. For large pressure gradients, the most rapid depth rotation occurs within the middle of the asthenospheric layer (Fig. 3A).

We also investigate the effects of varying the pressure gradient in the x_1 direction (α_1) while holding the transverse component of the pressure gradient (α_2) constant and non-zero (Fig. 3B). We find that as α_1 grows, the orientation of the strain axis moves closer to the orientation induced by pure Couette flow ($\theta = 0$). However, for large α_1, the shear caused by pressure gradients overwhelms the Couette component, and forces the strain axis to rotate rapidly in the mid-asthenosphere. Overall, the strain axis orientation will change with depth whenever the component of the pressure gradient transverse to plate motion is non-zero.

A similar analysis may be extended to Newtonian fluids with piecewise constant viscosity structure using the method presented in Section A1. In addition, we obtain analytical solutions to the Couette-Poiseuille flow model for a viscous fluid whose viscosity varies linearly with depth (Section A2), and for a non-Newtonian viscous fluid with constant pre-exponential rheological parameter (Section A3). In all of the above cases, we find that the orientation of the strain axis changes with depth as long as the pressure gradient transverse to the plate motion direction is non-zero. Thus, the presence of pressure-driven flow directed at an angle to plate motions may account for observations of depth-dependence of azimuthal seismic anisotropy in surface-wave tomography models (e.g. Becker *et al.* 2003; Debayle *et al.* 2005; Becker *et al.* 2007) and in GMFMs
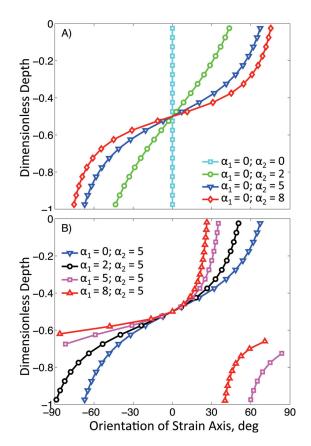

Figure 3. Analytical predictions of strain axis depth-rotation: (A) increasing pressure gradient transverse to plate motion (α_2) leads to progressively larger rotation of the strain axis in the asthenospheric layer; (B) the combination of pressure gradients parallel and orthogonal to plate motion (α_1 and α_2) induces different depth-rotations of the strain axis.

(e.g. Becker *et al.* 2003; Conrad *et al.* 2007; Conrad & Behn 2010, Fig. 2). Conversely, it should be possible to use the observations of azimuthal seismic anisotropy to quantify pressure-driven flow in the asthenosphere.

3 INVERTING FOR PRESSURE GRADIENTS

We use the depth profiles of the ISA orientations from the GMFM (Conrad *et al.* 2007; Conrad & Behn 2010) and strain axis rotations predicted by our analytical Couette-Poiseuille model with constant viscosity to constrain the range of possible horizontal pressure gradient magnitudes (α_i) and directions (θ_i) in the asthenospheric region of the GMFM, where viscosity is constant. This, in turn, allows us to easily quantify the relative contributions of Couette and Poiseuille flows to the total asthenospheric flow in the GMFM. This GMFM was developed using the spherical finite element code CitComS (Zhong *et al.* 2000; Tan *et al.* 2006). The GMFM uses NUVEL-1*A* plate motions (DeMets *et al.* 1994), mantle density heterogeneity computed from S20RTSb seismic tomography model (Ritsema *et al.* 2004) and net lithospheric rotation (Gripp & Gordon 2002) to drive the flow, and SKS splitting to constrain the relative influence of these drivers (Conrad *et al.* 2007; Conrad & Behn 2010). We take the orientations of the ISA, the thickness of the lithosphere, asthenospheric viscosity and mantle velocity at the base of the asthenosphere directly from the GMFM (Conrad & Behn 2010). We perform all of our calculations in the local reference frame of the mantle at 300 km. This choice is motivated by the original GMFM
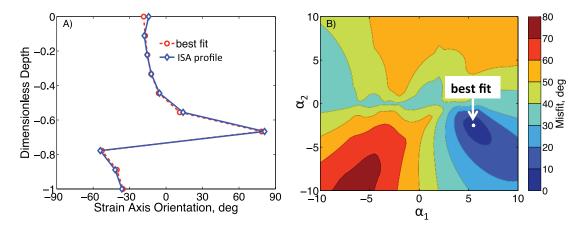
Figure 4. Inversion algorithm applied to a representative point (132.6°N, 45.8°W): (A) best-fitting profile closely matches the actual ISA depth profile; (B) the misfit surface as a function of α_1 and α_2 shows the pressure gradient value that minimizes the misfit for (A).

setup, where 300 km corresponds to the boundary between the lower viscosity asthenosphere and the higher viscosity upper mantle. To cast our calculations into the local reference frame of the mantle, we orient the x_1 axis at each grid point along the direction of the vector difference between observed plate motion and mantle flow at 300 km, let x_3 point up and choose x_2 so that the resulting coordinate system is right-handed. We then reorient the ISA at each point in each layer by subtracting the azimuth of the vector difference between the surface plate motion and mantle velocity at 300 km from the orientation of the ISA in each layer. We determine the thickness of the asthenosphere by subtracting the lithospheric thickness from 300 km. Since the vertical resolution of the GMFM is 25 km, the number of points in a depth profile of the ISA at a given point, N, is given by the quotient of the asthenospheric thickness (interpolated to the nearest available data layer) and 25 km.

At every GMFM surface grid point, we implement a grid search algorithm and find the values of α_1 and α_2 that produce the best fit to the observed depth rotation of the ISA in the asthenosphere of the GMFM. For the sake of computational parsimony, we restrict the α_1 and α_2 domains to lie between -10 and 10 dimensionless pressure gradient units. We quantify the misfit between the two curves by applying the root mean square (rms) function defined as

$$\text{misfit} = \sqrt{\sum_{i=1}^{N} \frac{(\phi_{o,i} - \phi_{a,i})^2}{N}}, \tag{9}$$

where $\phi_{o,i}$ is the orientation of the ISA from the GMFM at location i and $\phi_{a,i}$ is the strain axis orientation predicted by the analytical Couette-Poiseuille model for a given value of α_1 and α_2. We find the minimum misfit between the actual and analytical curves as a function of α_1 and α_2 at every grid point. Fig. 4 demonstrates the inversion results for an arbitrarily selected point. The misfits for the best-fitting points between the actual ISA orientation depth profile and the analytical profiles of the strain axis in the asthenosphere of the GMFM are generally low (average misfit of all grid points is 11°). We find that the misfits are highest (up to 35°) around plate boundaries, where flow may deviate significantly from plane Couette–Poiseuille approximation and the ISA may not be a valid predictor of the azimuthal seismic anisotropy.

Next, we dimensionalize α_1 and α_2 according to (4) and rotate them back into the reference frame of the Earth. Finally, we create a global map of horizontal pressure gradient magnitudes and directions everywhere in the asthenosphere (Fig. 5A). This map

reveals a number of disconnected regions with high values of the horizontal pressure gradient (up to about 30 Pa m^{-1}). Particularly, we find a high pressure gradient belt around the west coast of South America where the Nazca Plate is subducting. We also discover high pressure gradients near Australia where a continental keel is believed to be generating pressure gradients in the upper mantle (Harig *et al.* 2010). Notably, pressure gradients are high near mid-ocean ridges, the Eurasia/India Plate boundary and Western Eurasia, where they may be generated by subducted Tethys slab (Stampfli *et al.* 2002).

To test our method, we use the stress tensor from the GMFM to compute average horizontal pressure gradient magnitudes (α_{st}) and directions (θ_{st}) in the asthenosphere (Fig. 5B). A comparison of pressure gradient magnitudes and orientations obtained from our inversion method with those computed directly from the stress tensor reveals remarkable similarities in pressure gradient orientations (Fig. 6A), with 70 per cent of points deviating by less than 20°. Removing points that lie closer than 300 km from plate boundaries, which are not well-resolved in the GMFM (Conrad & Behn 2010), further improves the misfit (Fig. 6A). This strengthens the idea that the plane Couette–Poiseuille flow model adequately captures the flow dynamics throughout most of the asthenosphere, and justifies our approach.

However, we find that our inversion method on average underestimates the magnitudes of the pressure gradients (Fig. 6B) from the GMFM. While the average pressure gradient magnitude computed directly from the model stress tensor is 9.7 Pa m^{-1}, the average value of the pressure gradient obtained with our inversion algorithm is only 6.6 Pa m^{-1} (Fig. 5). This discrepancy can be explained by our implicit assumption that the asthenoshere hosts fully developed Poiseuille flow, which requires an infinite viscosity contrast between the asthenosphere and the upper mantle. Yet, in the GMFM the asthenosphere is only ten times less viscous than the upper mantle beneath it (Conrad *et al.* 2007; Conrad & Behn 2010). As a result, deformation of the upper mantle between 300 and 670 km depth in the GMFM accommodates a portion of the lateral pressure gradients.

To investigate whether upper mantle deformation could be a plausible explanation for the discrepancy in pressure gradient magnitudes and to explain the effect of removing points close to plate boundaries (Fig. 6), we develop a two-layer model that employs the numerical solution developed in Section A1. We create two sets of synthetic strain orientation depth-profiles for all combinations
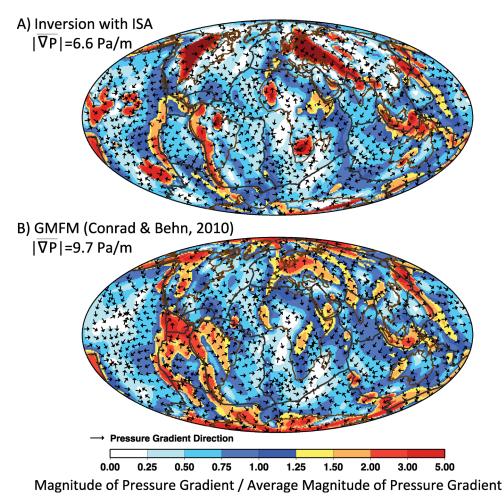
A) Inversion with ISA
$|\overline{\nabla P}|=6.6$ Pa/m

B) GMFM (Conrad & Behn, 2010)
$|\overline{\nabla P}|=9.7$ Pa/m

→ **Pressure Gradient Direction**

| 0.00 | 0.25 | 0.50 | 0.75 | 1.00 | 1.25 | 1.50 | 2.00 | 3.00 | 5.00 |

Magnitude of Pressure Gradient / Average Magnitude of Pressure Gradient

Figure 5. Pressure gradient magnitudes (colours) and directions (arrows): (A) obtained using the inversion algorithm; (B) computed directly from the GMFM stress tensor.

of α_1 and α_2 in our domain, using viscosity contrasts between the asthenosphere (200 km thick) and the layer beneath it (370 km thick) of 10 and 100. We then compare these solutions to solutions in which we assume a single layer with an infinite viscosity contrast. We find that a viscosity contrast of only 10 causes our inversion routine to distort the magnitude (up to a factor of 4) and the orientation (up to 40°) of pressure gradients within a significant portion of our domain (Figs 7A and C). Examining the 2-D histogram of α_1 and α_2 obtained using either inversion method (Fig. 8D) or the GMFM stress tensor (Fig. 8C) reveals that the majority of the points in the GMFM have pressure gradient values that lie to the right of the $\alpha_1 = 0$ line in the numerical domain (i.e. in the direction of plate motion), a region where a too-small viscosity contrast leads our algorithm to underestimate the magnitude of pressure gradients (Fig. 7A). Hence, the presence of a relatively small viscosity contrast in the GMFM (factor of 10) explains why our predicted pressure gradients are on average smaller than those actually present in the GMFM asthenosphere. Still, some points lie within the portion of the domain where our algorithm overestimates the magnitude of pressure gradients (e.g. $\alpha_1 < 0$ in Fig. 7A), which explains why some of our predictions are too high. Importantly, we find that the presence of a higher viscosity contrast (e.g. a factor of 100) significantly improves the performance of our inversion algorithm (Figs 7B and D).

A possible explanation for why removing points close to plate boundaries increases the magnitude of predicted pressure gradients

slightly (Fig. 6B) lies in the pressure field distribution around these regions. At the divergent margins, we expect pressure to be minimized close to the ridge axis as the plates move apart. Thus, α_1 around divergent margins should be positive. At convergent margins, we also expect α_1 to be positive as pressure increases near points of convergence in models with imposed velocity boundary conditions (Hager & O'Connell 1979). Hence, omitting points close to plate boundaries from our analysis should result in preferential removal of points where our algorithm tends to underestimate pressure gradient magnitudes (Fig. 7A), which also leads to an increase in the relative number of points at which we overestimate pressure gradient magnitude.

In general, the pressure gradients obtained using our inversion method deviate from the GMFM output in the areas where the plane Couette–Poiseuille flow model is not expected to be a good approximation of flow dynamics. For example, plate boundaries are likely dominated by more complex flow regimes where vertical velocities may not be neglected (e.g. Turcotte & Schubert 1967). In addition, we find large misfits between the GMFM pressure gradients and our results (Fig. 5) in regions of known mantle upwellings and downwellings. Particularly, the orientations of pressure gradients poorly match in the middle of the North American continent, where the subducted Farallon slab is believed to be driving large vertical flow (Conrad *et al.* 2004; Forte *et al.* 2007). We also discover a region of large discrepancy below Eurasia, where the Tethys slab is probably sinking (Stampfli *et al.* 2002), and thus creating significant
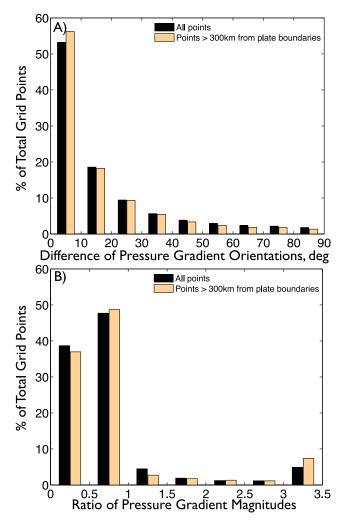
Figure 6. Distribution of (A) angular difference ($|\theta - \theta_{st}|$) and (B) magnitude ratio of horizontal pressure gradients ($\frac{\theta}{\theta_{st}}$) in the asthenosphere obtained using inversion method (θ) compared to those computed directly from the stress tensor of the global numerical mantle flow model (θ_{st}). Dark bars show results for all grid points; light bars exclude points within 300 km of a plate boundary.

deviations from an idealized plane Couette–Poiseuille flow. Finally, misfits beneath cratons are likely caused by an inadequate number of resolved layers (25 km spacing) within the thin subcratonic asthenosphere.

4 ROBUSTNESS OF THE INVERSION ALGORITHM

To verify the stability of our algorithm and further test our results, we perform a sensitivity analysis. For each combination of dimensionless α_1 and α_2, we run 300 realizations of the grid search algorithm on analytical profiles of depth-rotated anisotropy (e.g. as in Fig. 3) that have been randomly perturbed at each depth by $\pm 18°$ using a uniform distribution, which corresponds to adding 20 per cent noise to the data. We then attempt to recover the original α_1, α_2 using our inversion routine.

The sensitivity analysis reveals that our algorithm is relatively stable everywhere in our chosen domain except for cases where the component of pressure gradient transverse to plate motion is close

to zero (Figs 8A and B). The standard deviation of the pressure gradient magnitudes and orientations shows less then 20 per cent variation in magnitude (Fig. 8A) and less than about 10° variation in orientation (Fig. 8B), except near $\alpha_2 = 0$. The maximum error in the orientation of pressure gradient is $\sim 40°$ and occurs for very small pressure gradients (Fig. 8B). This happens because simple shear orientations produced by Couette and Poiseuille flows point in the same direction if pressure gradients transverse to plate motion are zero. In such situations, we are unable to make any inferences about the magnitude of the pressure gradient (except that $\alpha_2 = 0$).

5 DISCUSSION: QUANTIFYING POISEUILLE FLOW

To quantify the relative importance of Couette and Poiseuille flows, we separate the net asthenospheric flow in the GMFM into components driven by each flow type. In particular, we use (7) to compute the average Poiseuile velocity at every point on the grid. We obtain an expression for Couette velocity by setting α_1 and α_2 in (7) to zero:

$$U_{1C}(X_3) = X_3 + 1 \tag{10a}$$

$$U_{2C}(X_3) = 0. \tag{10b}$$

The Poiseulle velocity is then given by

$$U_{1P}(X_3) = \frac{1}{2}\alpha_1\left(X_3^2 + X_3\right) \tag{11a}$$

$$U_{2P}(X_3) = \frac{1}{2}\alpha_2\left(X_3^2 + X_3\right). \tag{11b}$$

Averaged through the layer, we find that the average Couette velocity in the asthenosphere is

$$\bar{U}_{1C} = \frac{1}{2} \tag{12a}$$

$$\bar{U}_{2C} = 0 \tag{12b}$$

while the average Poiseuille velocity is found to be

$$\bar{U}_{1P} = -\frac{1}{12}\alpha_1 \tag{13a}$$

$$\bar{U}_{2P} = -\frac{1}{12}\alpha_2. \tag{13b}$$

By plotting Poiseuille flow as a percentage of total flow (computed as $\frac{(U_{1P}^2 + U_{2P}^2)^{1/2}}{((U_{1P}+U_{1C})^2 + U_{2P}^2)^{1/2}}$) (Fig. 9), we show that a significant proportion of the Earth's asthenospheric flow (as defined in the GMFM) is driven by lateral pressure gradients (nearly 40 per cent on average). The asthenosphere beneath central North America and the west coast of South America is dominated by Poiseuille flow generated by upwelling and subduction, respectively. Asthenospheric flow beneath Australia also shows evidence of pressure-driven flow, which is likely amplified by the continental keel (Harig *et al.* 2010). We also find a significant Poiseuille component of the flow beneath the East Pacific Rise and the Mid-Atlantic Ridge. Finally, we observe that Poiseuille flow is important around Hawaii and Southeast Africa, where mantle upwellings may be responsible for generating pressure gradients (Wolfe *et al.* 2009; Moucha & Forte 2011).
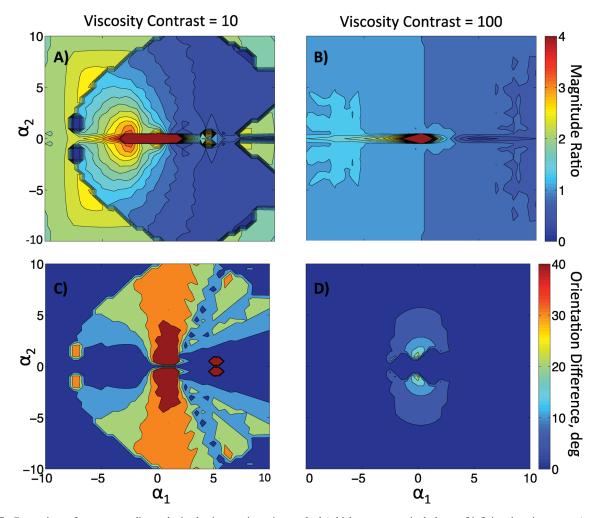
Figure 7. Comparison of pressure gradients obtained using our inversion method (which assumes a single layer of infinite viscosity contrast) to pressure gradients used to predict depth rotation in a two layer model (Section A1) for all pressure gradient combinations (α_1 and α_2) in the domain, in increments of 0.5. The two layer model includes a 200 km thick asthenosphere and a 370 km thick upper mantle that is either 10 (A and C) or 100 (B and D) times more viscous than the asthenosphere. Shown are (A and B) the magnitude ratios of inverted to applied pressure gradients, and (C and D) the angular difference in pressure gradient orientations.

In the future, a plane Couette–Poiseuille flow model could be used in conjunction with observations of depth rotation of azimuthal seismic anisotropy to invert for horizontal pressure gradients in the Earth's asthenosphere. While global azimuthal seismic anisotropy models may suffer from resolution issues, high resolution regional azimuthal anisotropy models (e.g. Marone & Romanowicz 2007; Deschamps *et al.* 2008; Hansen *et al.* 2008; Lin *et al.* 2010; Yuan & Romanowicz 2010) use the depth-sensitivity of frequency-dependent surface waves to constrain the depth variation of anisotropy; these tomographic models should be useful for constraining pressure gradients in Earth's asthenosphere.

However, to most usefully apply our method to such constraints, it will be necessary to account for several factors. First, we expect the pressure gradient field in the asthenosphere to be spatially smooth over lateral distances of at least hundreds of kilometres (away from plate boundaries). Hence, using an inversion algorithm that can ensure spatial coherence of pressure gradients will help improve our method's applicability by utilizing combined constraints on depth-rotation across broad regions. Secondly, current uncertainties in the location of the lithosphere–asthenosphere boundary need to be reduced to distinguish depth-rotations asso-

ciated with asthenospheric pressure gradients from those caused by differences between the anisotropic fabrics of the lithosphere and asthenosphere. Thirdly, it may be necessary to invert for additional parameters, such as the thickness of the asthenosphere, mantle flow velocity beneath the base of the asthenosphere and the asthenospheric viscosity structure, because these parameters are poorly constrained in places, and it is not clear that input values should be taken from numerical flow models. Hence, depth-dependence of seismic anisotropy may additionally provide a new constraint on these parameters. However, realizing these constraints will require more and better seismic data, and may introduce new trade-offs. Finally, because much of the upper 400 km of the mantle is dominated by dislocation creep (Karato & Wu 1993), using a Couette-Poiseuille solution for a non-Newtonian fluid could be more appropriate (Section A3), despite added complexity and computational cost.

6 CONCLUSIONS

Using analytical solutions of the Navier-Stokes equations for a variety of asthenospheric viscosity structures (Newtonian fluid
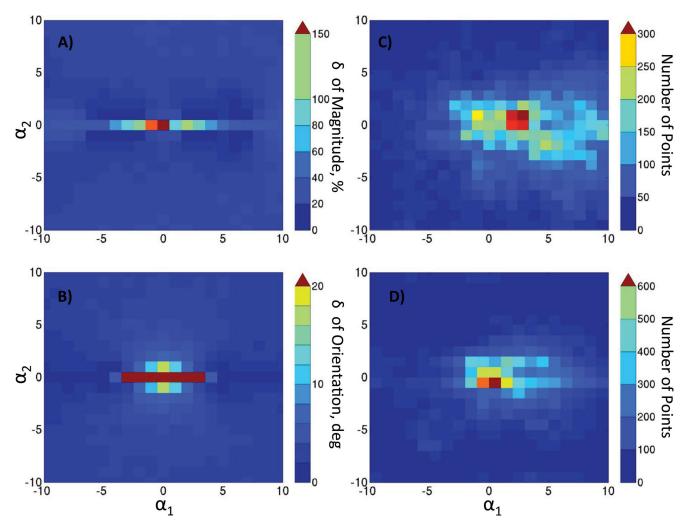
Figure 8. Sensitivity analysis: Mean standard deviation of (A) dimensionless pressure gradient magnitudes as a percentage of true magnitude, and (B) pressure gradient orientations, after 300 realizations that include 20 per cent noise; (C) 2-D histogram of pressure gradients in the GMFM computed from the stress tensor; (D) 2-D histogram of pressure gradients obtained using the inversion method.

with constant or depth-dependent viscosity, or a non-Newtionian fluid with constant pre-exponential rheological parameter), we show that the strain axis (and presumably also azimuthal seismic anisotropy) will change orientation with depth in the presence of a pressure gradient with a component orthogonal to plate motion. This finding suggests that depth variations in the orientation of azimuthal seismic anisotropy should result from pressure-driven asthenopsheric flow. These depth-rotations are most rapid in the middle of the asthenospheric layer (Fig. 3), which should make them distinct from depth-variations associated with fabric differences between asthenospheric and lithospheric layers (Deschamps *et al.* 2008; Gao *et al.* 2010; Huang *et al.* 2011; Vinnik *et al.* 2012). We demonstrate here that this depth-rotation can be used to constrain the magnitude and direction of pressure gradients in the asthenosphere. In particular, we develop an inversion scheme for accomplishing this, and test it on a synthetic case represented by a numerical mantle flow model (Conrad & Behn 2010). We find that for most of the asthenosphere our inversion scheme constrains the orientation and, to a lesser extent, the magnitude of asthenospheric pressure gradients. Our inversion method fails in locations where Poiseuille flow is nearly parallel to plate motions, and in locations where mantle dynamics may not be adequately captured by

the plane Couette–Poiseuille approximation (e.g. plate boundaries, cratons and areas of significant upwelling or downwelling).

For a global mantle flow model, we find that Poiseuille flow dominates asthenospheric flow where pressure gradients are largest, such as near mid-ocean ridges and above areas of known upwelling and downwelling, particularly on the Atlantic side of the world where plate motions, and therefore Couette flows, are slower. By contrast, Couette flow is more important beneath the fast-moving plates of the Pacific basin (Fig. 9). We estimate that Poiseuille flow constitutes about 40 per cent of the total flow velocity amplitude on average, which suggests that pressure-driven flow is an important component of asthenospheric dynamics in the numerical flow model (Conrad & Behn 2010). A straightforward application of our method to actual observations of depth-rotation (obtained from frequency-dependent surface wave tomography models) may be tricky given current uncertainties in asthenospheric viscosity structure, thickness and rheology, as well as possible data resolution issues. Nonetheless, our work offers a new framework for interpreting observations of depth-dependence of azimuthal seismic anisotropy in the asthenosphere and provides a method to constrain, at least in principle, the pressure-driven component of horizontal flow in the asthenosphere.
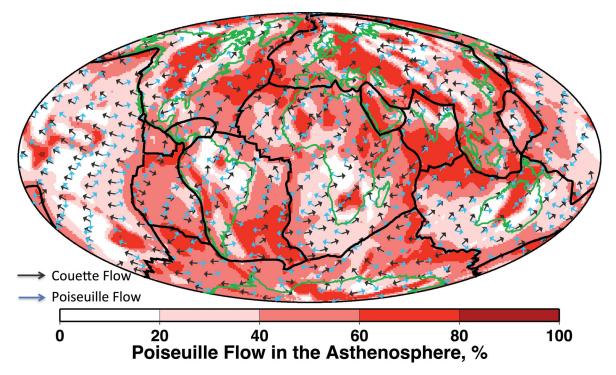
Figure 9. Magnitude of Poiseuille flow velocity in the asthenosphere obtained using the inversion method as a percentage of total flow velocity (colours). Arrows show the orientations of Couette (black) and Poiseuille (blue) flows.

REFERENCES

Batchelor, G.K., 1967. *Fluid Dynamics,* Cambridge University Press, New York, NY.

Becker, T.W., Chevrot, S., Schulte Pelkum, V. & Blackman, D.K., 2006a. Statistical properties of seismic anisotropy predicted by upper mantle geodynamic models, *J. geophys. Res.,* **111,** B08309, doi:10.1029/2005JB004095.

Becker, T.W., Ekström, G., Boschi, L. & Woodhouse, J., 2007. Length scales, patterns, and origin of azimuthal seismic anisotropy in the upper mantle as mapped by Rayleigh Waves, *Geophys. J. Int.,* **171,** 451–462.

Becker, T.W., Kellogg, J.B., Ekström, G. & O'Connell, J.R., 2003. Comparison of azimuthal seismic anisotropy from surface waves and finite strain from global mantle-circulation models, *Geophys. J. Int.,* **155,** 696–714.

Becker, T.W., Schulte Pelkum, V., Blackman, D.K., Kellogg, J.B. & O'Connell, R.J., 2006b. Mantle flow under the western United States from shear wave splitting, *Earth planet. Sci. Lett.,* **247,** 235–251.

Behn, M.D., Conrad, C.P. & Silver, P.G., 2004. Detection of upper mantle flow associated with the african superplume, *Earth planet. Sci. Lett.,* **224,** 259–274.

Conder, J.A., Forsyth, D.W. & Parmentier, E.M., 2002. Asthenospheric flow and asymmetry of the East Pacific Rise, MELT area, *J. geophys. Res.,* **107**(B12), doi:10.1029/2001JB000807.

Conrad, C.P. & Behn, M.D., 2010. Constraints on lithosphere net rotation and asthenospheric viscosity from global mantle flow models and seismic anisotropy, *Geochem. Geophys. Geosyst.,* **11,** Q05W05, doi:10.1029/2009GC002970.

Conrad, C.P., Behn, M.D. & Silver, P.G., 2007. Global mantle flow and the development of seismic anisotropy: differences between the oceanic and continental upper mantle, *J. geophys. Res.,* **112,** B07317, doi:10.1029/2006JB004608.

Conrad, C.P., Bianco, T.A., Smith, E.I. & Wessel, P., 2011. Patterns of intraplate volcanism controlled by asthenospheric shear, *Nat. Geosci.,* **4,** 317–321.

Conrad, C.P., Lithgow-Bertelloni, C. & Louden, K.E., 2004. Iceland, the Farallon slab, and dynamic topography of the North Atlantic, *Geology,* **32,** 177–180.

Couette, M., 1890. Études sur le frottement des liquides, *Ann. Chim. Phys.,* **21,** 433–510.

Crowley, J.W. & O'Connell, R.J., 2012. An analytic model of convection in a system with Layered viscosity and plates, *Geophys. J. Int.,* **188,** 61–78, doi:10.1111/j.1365-246X.2011.05254.x.

Debayle, E., Kennett, B. & Priestley, K., 2005. Global azimuthal seismic anisotropy and the unique plate-motion deformation of Australia, *Nature,* **443,** 509–512.

DeMets, C., Gordon, G., Argus, D.F. & Stein, S., 1994. Effect of recent revisions to the geomagnetic reversal time scale on estimates of current plate motions, *Geophys. Res. Lett.,* **21,** 2191–2194.

Deschamps, F., Lebedev, S., Meier, T. & Trampet, J., 2008. Stratified seismic anisotropy reveals past and present deformation beneath the east-central United States, *Earth planet. Sci. Lett.,* **274,** 489–498.

Forte, A.M., Mitrovica, J.X., Moucha, R., Simmons, N.A. & Grand, S.P., 2007. Descent of the ancient Farallon slab drives localized mantle flow below the New Madrid seismic zone, *Geophys. Res. Lett.,* **34,** L04308, doi:10.1029/2006GL027895.

Gaboret, C., Forte, A.M. & Montagner, J.P., 2003. The unique dynamics of the pacific hemisphere mantle and its signature on seismic anisotropy, *Earth planet. Sci. Lett.,* **208,** 219–233.

Gao, S., Liu, K.H. & Abdelsalam, M.G., 2010. Seismic anisotropy beneath the afar depression and adjacent areas: implications for mantle flow, *J. geophys. Res.,* **115,** B12330, doi:10.1029/2009JB007141.

Gripp, A.E. & Gordon, R.G., 2002. Young tracks of hotspots and current plate velocities, *Geophys. J. Int.,* **150,** 321–361.

Hager, B.H. & O'Connell, R.J., 1979. Kinematic models of large-scale flow in the earth's Mantle, *J. geophys. Res.,* **84,** 1031–1048.

Hager, B.H. & O'Connell, R.J., 1981. A simple global model of plate dynamics and mantle convection, *J. geophys. Res.,* **86**(364), 4843–4867.

Hammond, J.O.S., Kendall, J.M., Rumpker, G., Wookey, J., Teanby, N., Joseph, P., Ryberg, T. & Stuart, G., 2005. Upper mantle anisotropy beneath the Seychelles Microcontinent, *J. geophys. Res.,* **110**, B11401, doi:10.1029/2005JB003757.

Hansen, S.E., Gaherty, J.B., Schwartz, S.Y., Rodgers, A.J. & Al Amri, A.M.S., 2008. Seismic velocity structure and depth-dependence of anisotropy in the Red Sea and Arabian shield from surface wave analysis, *J. geophys. Res.,* **113**, B10307, doi:10.1029/2007JB005335.

Harig, C., Zhong, S. & Simons, F.J., 2010. Constraints on upper mantle viscosity from the flow-induced pressure gradient across the Australia continental keel, *Geochem. Geophys. Geosyst.,* **1**(6), Q06004, doi:10.1029/2010GC003038.

Höink, T. & Lenardic, A., 2010. Wavelength convection, Poiseuille-Couette flow in the low viscosity asthenosphere and the strength of plate margins, *Geophys. J. Int.,* **180**, 23–33.

Huang, Z., Wang, L., Zhao, D., Mi, N. & Xu, M., 2011. Seismic anisotropy and mantle dynamics beneath China, *Earth planet. Sci. Lett.,* **306**, 105–117.

Kaminski, E. & Ribe, N.M., 2002. Timescales for the evolution of seismic anisotropy in mantle flow, *Geochem. Geophys. Geosyst.,* **3**(1), doi:10.1029/2001GC000222.

Karato, S., 2012. On the origin of the asthenosphere, *Earth planet. Sci. Lett.,* **321–322**, 95–103.

Karato, S. & Wu, P., 1993. Rheology of the upper mantle: a synthesis, *Science,* **260**, 771–778.

Korenaga, J., 2008. Comment on "Intermittent Plate Tectonics?", *Science,* **320**, 5881, doi:10.1126/science.1155214.

Lai, W., Rubin, D. & Krempl, E., 2010. Introduction to Continuum Mechanics, 4th edn, Elsevier, Burlington, MA.

Lenardic, A., Richards, M.A. & Busse, F.H., 2006. Depth-dependent rheology and the horizontal length-scale of mantle convection, *J. geophys. Res.,* **111**, B07404, doi:10.1029/2005JB003639.

Lin, F.C., Ritzwoller, M.H., Yang, Y., Moschetti, M.P. & Fouch, M.J., 2010. Complex and variable crustal and uppermost mantle seismic anisotropy in the Western United States, *Nat. Geosci.,* **4**, 55–61, doi:10.1038/ngeo1036.

Long, M.D. & Silver, P.G., 2009. Mantle flow in subduction systems: the subslab flow field and implications for mantle dynamics, *J. geophys. Res.,* **114**, B10312, doi:10.1029/2008JB006200.

Marone, F. & Romanowicz, B., 2007. The depth distribution of azimuthal anisotropy in the continental upper mantle, *Nature,* **447**, 198–201.

McKenzie, D., 1979. Finite deformation during fluid flow, *Geophys. J. R. astr. Soc.,* **58**, 689–715.

Moucha, R. & Forte, A.M., 2011. Changes in african topography driven by mantle convection, *Nat. Geosci.,* **4**, 707–712.

Papanastasiou, T.C., Georgiou, G.C. & Alexandrou, A.N., 2000. *Viscous Fluid Flow,* CRP Press, Boca Raton, FL.

Phipps Morgan, J., Hasenclever, J., Hort, M., Rüpke, L. & Parmentier, E.M., 2007. On subducting slab entrainment of buoyant asthenosphere, *Terra Nova,* **19**, 167–172.

Phipps Morgan, J., Morgan, W.J., Zhang, Y.S. & Smith, W.H.E., 1995. Observational hints for a plume-fed, suboceanic asthenosphere and its role in mantle convection, *J. geophys. Res.,* **100**(B7), 12 753–12 767.

Phipps Morgan, J. & Smith, W.H.F., 2002. Flattening of the seafloor depth-age curve as a response to asthenospheric flow, *Nature,* **359**, 524–527.

Poiseuille, J.L.M., 1840a. Recherches expérimentales surle mouvement des liquides dans les tubes de trés petits diametres, *C. R. Acad. Sci. Paris,* **11**, 961–967.

Poiseuille, J.L.M., 1840b. Recherches expérimentales surle mouvement des liquides dans les tubes de trés petits diametres, *C. R. Acad. Sci. Paris,* **11**, 1041–1048.

Poiseuille, J.L.M., 1840c. Recherches expérimentales surle mouvement des liquides dans les tubes de trés petits diametres, *C. R. Acad. Sci. Paris,* **12**, 112–115.

Ribe, N.M., 1989. Seismic anisotropy and mantle flow, *J. geophys. Res.,* **94**, 4213–4223.

Ricard, Y., Froidevaux, C. & Fleitout, L., 1988. Global plate motion and the geoid: a physical model, *Geophys. J. Int.,* **93**, 477–484.

Richards, M.A., Yang, W., Baumgardner, J.R. & Bunge, H., 2001. Role of a low-viscosity zone in stabilizing plate tectonics: implications for comparative terrestrial planetology, *Geochem. Geophys. Geosyst.,* **2**, 1026, doi:10.1029/2000GC000115.

Ritsema, J., van Heijst, H.J & Woodhouse, J.H., 2004. Global transition zone tomography, *J. geophys. Res.,* **109**, B02302, doi:10.1029/2003JB002610.

Ryan, M.P., 1990. *Magma Transport and Storage,* John Wiley and Sons Ltd, San Francisco, CA.

Savage, M.K., 1999. Seismic anisotropy and mantle deformation: what have we learned from shear wave splitting?, *Rev. Geophys.,* **37**, 65–106.

Savage, M.K. & Holt, W.E., 2002. The mantle flow field beneath Western North America, *Science,* **295**, 1054–1057.

Silver, P.G. & Behn, M.D., 2008. Intermittent plate tectonics? *Science,* **319**, 85–88.

Solomatov, V., 1995. Scaling of temperature and stress-dependent viscosity convection, *Phys. Fluids,* **7**(2), 266–274.

Stampfli, G.M., Von Raumer, J.F. & Borel, G.D., 2002. Paleozoic evolution of pre-Variscan terranes: from Gondwana to the Variscan Collision, *Geol. Soc. Am.,* **364**, 263–280.

Tan, E., Choi, E., Thoutireddy, P., Gurnis, M. & Aivazis, M., 2006. GeoFramework: coupling multiple models of mantle convection within a computational framework, *Geochem. Geophys. Geosyst.,* **7**, Q06001, doi:10.1029/2005GC001155.

Toomey, D.R., Wilcock, W.S.D., Conder, J.A., Forsyth, D.W., Blundy, J.D., Parmentier, E.M. & Hammond, W.C., 2002. Asymmetric mantle dynamics in the MELT region of the East Pacific Rise, *Earth planet. Sci. Lett.,* **200**, 287–295.

Turcotte, D.L. & Schubert, G., 1967. *Geodynamics,* Cambridge University Press, New York, NY.

van Summeren, J., Conrad, C.P. & Lithgow-Bertelloni, C., 2012. The importance of weak slabs and a global asthenosphere to plate motion, *Geochem. Geophys. Geosyst.,* 13, doi:10.1029/2011GC003873.

Vinnik, L., Kiselev, S., Weber, M., Oreshin, S. & Makeyeva, L., 2012. Frozen and active seismic anisotropy beneath southern Africa, *Geophys. Res. Lett.,* **39**, 8, doi:10.1029/2012GL051326.

Wolfe, C.J., Solomon, S.C., Laske, G., Collins, J.A., Detrick, R.S., Orcutt, J.A., Bercovici, D. & Hauri, E.H., 2009. Mantle shear-wave velocity structure beneath the Hawaiian hot spot, *Science,* **326**, 1388–1390.

Yamamoto, M., Morgan, J.P. & Morgan, W.J., 2007. Global plume-fed asthenosphere flow - I: motivation and model development, *Geol. Soc. Am.,* **430**, 165–188, doi:10.1130/2007.2430(09).

Yuan, H. & Romanowicz, B., 2010. Depth dependent azimuthal anisotropy in the Western US upper mantle, *Earth planet. Sci. Lett.,* **300**, 385–394.

Zhong, S., Zuber, M.T., Moresi, L.N. & Gurnis, M., 2000. The role of temperature dependent viscosity and surface plates in spherical shell models of mantle convection, *J. geophys. Res.,* **105**(B5), doi:10.1029/2000JB900003.

APPENDIX

A1 Newtonian 2-D Couette Poiseuille flow in *N* layers with layered viscosity structure—numerical approach

To address the case of a viscous fluid with a layered viscosity structure, we employ a numerical approach. Let us partition the asthenosphere into *N* layers. Let the viscosity of the top layer be μ_1 and the viscosity of the *N*th layer be μ_N. The solution to the governing system of eq. (2) for the *n*th layer is given by

$$U_{1,n}(X_{3,n}) = \frac{1}{2}\alpha_{1,n}X_{3,n}^2 + A_{1,n}X_{3,n} + A_{2,n} \tag{A1a}$$

$$U_{2,n}(X_{3,n}) = \frac{1}{2}\alpha_{2,n}X_{3,n}^2 + B_{1,n}X_{3,n} + B_{2,n}. \tag{A1b}$$

The conditions at the interfaces are the continuity of velocities and stresses (e.g. Lai *et al.* 2010). We will first address the solution for the X_1 component. The continuity of velocities across the nth interface can be described as

$$U_{1,n}\big|_{X_{3,n}} = U_{1,n+1}\big|_{X_{3,n}}. \tag{A2}$$

Thus,

$$A_{1,n}X_{3,n} + A_{2,n} - A_{1,n+1}X_{3,n} - A_{2,n+1} = \frac{1}{2}X_{3,n}^2\left(\alpha_{1,n+1} - \alpha_{1,n}\right). \tag{A3}$$

The continuity of stresses across the nth interface is given by

$$\mu_n \left.\frac{\partial U_{1,n}}{\partial X_3}\right|_{X_{3,n}} = \mu_{n+1} \left.\frac{\partial U_{1,n}}{\partial X_3}\right|_{X_{3,n}}, \tag{A4}$$

which gives

$$\mu_n A_{1,n} - \mu_{n+1} A_{1,n+1} = X_{3,n}\left(\mu_{n+1}\alpha_{1,n+1} - \mu_n\alpha_{1,n}\right). \tag{A5}$$

We combine (A3), (A5) and (3) (Hager & O'Connell 1981) to obtain the following system of linear equations for the x_1 component:

$$M\vec{A} = \vec{x}_1, \tag{A6}$$

which may be expanded as

$$M = \begin{pmatrix}
0 & 1 & 0 & \cdots & \cdots & \cdots & \cdots & \cdots \\
X_{3,1} & 1 & -X_{3,1} & -1 & 0 & \cdots & \cdots & \cdots \\
0 & 0 & X_{3,2} & 1 & -X_{3,2} & -1 & 0 & \cdots \\
\vdots & \vdots & \vdots & \vdots & \vdots & \vdots & \vdots & \vdots \\
\mu_1 & 0 & -\mu_2 & 0 & \cdots & \cdots & \cdots & \cdots \\
0 & 0 & \mu_2 & 0 & -\mu_3 & 0 & \cdots & \cdots \\
\vdots & \vdots & \vdots & \vdots & \vdots & \vdots & \vdots & \vdots \\
\cdots & \cdots & \cdots & \cdots & \cdots & \cdots & 1 & -1
\end{pmatrix}, \tag{A7}$$

$$\vec{A} = \begin{pmatrix}
A_{1,1} \\
A_{2,1} \\
A_{1,2} \\
A_{2,2} \\
\vdots \\
\vdots \\
A_{1,N} \\
A_{2,N}
\end{pmatrix}, \tag{A8}$$

and

$$\vec{x}_1 = \begin{pmatrix}
1 \\
\frac{1}{2}X_{3,1}^2\left(\alpha_{1,2} - \alpha_{1,1}\right) \\
\frac{1}{2}X_{3,2}^2\left(\alpha_{1,3} - \alpha_{1,2}\right) \\
\vdots \\
X_{3,1}\left(\mu_2\alpha_{1,2} - \mu_1\alpha_{1,1}\right) \\
X_{3,2}\left(\mu_3\alpha_{1,3} - \mu_2\alpha_{1,2}\right) \\
\vdots \\
\frac{1}{2}\alpha_{1,N}
\end{pmatrix}. \tag{A9}$$

Applying similar reasoning, we derive a linear system of equations for the x_2 component

$$M\vec{B} = \vec{x}_2, \tag{A10}$$

where matrix M is as above,

$$\vec{B} = \begin{pmatrix}
B_{1,1} \\
B_{2,1} \\
B_{1,2} \\
B_{2,2} \\
\vdots \\
\vdots \\
B_{1,N} \\
B_{2,N}
\end{pmatrix} \tag{A11}$$

and

$$\vec{x}_2 = \begin{pmatrix}
0 \\
\frac{1}{2}X_{3,1}^2\left(\alpha_{2,2} - \alpha_{2,1}\right) \\
\frac{1}{2}X_{3,2}^2\left(\alpha_{2,3} - \alpha_{2,2}\right) \\
\vdots \\
X_{3,1}\left(\mu_2\alpha_{2,2} - \mu_1\alpha_{2,1}\right) \\
X_{3,2}\left(\mu_3\alpha_{2,3} - \mu_2\alpha_{2,2}\right) \\
\vdots \\
\frac{1}{2}\alpha_{2,N}
\end{pmatrix}. \tag{A12}$$

Once M is inverted using standard schemes, $\vec{A}$ and $\vec{B}$ may be determined using (A6) and (A10). Finally, (A1) and its derivative may then be used to compute the pressure gradient magnitudes and directions for fluids with a layered viscosity structure.

A2 Couette–Poiseuille flow with Newtonian rheology and linearly varying depth-dependent viscosity

We treat the upper mantle as a Newtonian fluid where viscosity is allowed to vary linearly with depth, i.e.

$$\mu = \mu_o\left(1 + \gamma x_3\right), \tag{A13}$$

and where γ is an arbitrary constant that controls the rate and sense of change of viscosity. The governing system of eq. (1) may then be written as

$$-\frac{\partial p}{\partial x_1} + \frac{\partial}{\partial x_3}\left(\mu_o(1+\gamma x_3)\frac{\partial u_1(x_3)}{\partial x_3}\right) = 0 \tag{A14a}$$

$$-\frac{\partial p}{\partial x_2} + \frac{\partial}{\partial x_3}\left(\mu_o(1+\gamma x_3)\frac{\partial u_2(x_3)}{\partial x_3}\right) = 0. \tag{A14b}$$

The non-dimensionalized analogue of (A14) is

$$-\alpha_1 + \frac{\partial}{\partial X_3}\left((1+\gamma^* X_3)\frac{\partial U_1(X_3)}{\partial X_3}\right) = 0 \tag{A15a}$$

$$-\alpha_2 + \frac{\partial}{\partial X_3}\left((1+\gamma^* X_3)\frac{\partial U_2(x_3)}{\partial X_3}\right) = 0, \tag{A15b}$$

where U, X_3, P_1 and P_2 are defined by (4) and

$$\gamma^* = \gamma H. \tag{A16}$$

Again, α_1 and α_2 are the non-dimensionalized parameters that determine the horizontal pressure gradient in the X_1 and X_2 directions, as in the case of constant viscosity. The magnitude and orientation of the pressure gradient are given by (5) and (6). Solving (A15) gives

$$U_1(X_3) = \frac{(C_1\gamma^* - \alpha_1)\ln(\gamma^* X_3 + 1) + \alpha_1\gamma^* X_3}{\gamma^{*2}} + C_2 \tag{A17a}$$

$$U_2(X_3) = \frac{(D_1\gamma^* - \alpha_2)\ln(\gamma^* X_3 + 1) + \alpha_2\gamma^* X_3}{\gamma^{*2}} + D_2. \tag{A17b}$$

Applying boundary conditions described in (3), we find the unknown constants of integration:

$$C_1 = \frac{(\alpha_1 - \gamma^*)}{\ln(1-\gamma^*)} + \frac{\alpha_1}{\gamma^*} \tag{A18}$$

$$C_2 = 1 \tag{A19}$$

$$D_1 = \frac{\alpha_2 - \gamma^*}{\ln(1-\gamma^*)} + \frac{\alpha_2}{\gamma^*} \tag{A20}$$

$$D_2 = 0 \tag{A21}$$

In the limit as γ^* approaches zero, we recover the solution for a Newtonian fluid with depth independent viscosity given by (7). Next, we differentiate (A17) with respect to X_3 to compute the strain rate with depth

$$\frac{dU_1}{dX_3} = \frac{(C_1\gamma^* - \alpha_1)}{(\gamma^* X_3 + 1)\gamma^*} + \frac{\alpha_1}{\gamma^*} \tag{A22a}$$

$$\frac{dU_2}{dX_3} = \frac{(D_1\gamma^* - \alpha_2)}{(\gamma^* X_3 + 1)\gamma^*} + \frac{\alpha_2}{\gamma^*}. \tag{A22b}$$

Expression (A22) gives the orientation of the shear in the layer.

A3 Non-Newtonian 2-D Couette Poiseuille flow: constant pre-exponential rheological parameter

Here we treat the asthenosphere as a non-Newtonian fluid. This means that the relationship between stress and strain is no longer linear. Instead, the power-law rheology is described by

$$\tau = \frac{1}{C\tau_{II}^{n-1}}\dot{\epsilon}, \tag{A23}$$

where C is a pre-exponential rheological parameter, $1/C\tau^{n-1}$ is the effective viscosity and τ_{II} is the second invariant of stress tensor. Here, we use

$$\tau_{II}^2 = \tau_{13}^2 + \tau_{23}^2, \tag{A24}$$

which is the simplest case for which only shear terms are significant. We consider the case of $n = 3$, which is appropriate for disclocation creep in olivine (Karato & Wu 1993). Then, for a non-Newtonian fluid with constant pre-exponential rheological parameter C, (A23) becomes

$$\dot{\epsilon}_{13} = C\left(\tau_{13}^2 + \tau_{23}^2\right)\tau_{13} = \frac{du_1}{dx_3} \tag{A25a}$$

$$\dot{\epsilon}_{23} = C\left(\tau_{13}^2 + \tau_{23}^2\right)\tau_{23} = \frac{du_2}{dx_3}. \tag{A25b}$$

Integrating (1) with respect to x_3 gives

$$\tau_{13} = C_1 + \frac{\partial p}{\partial x_1}x_3 \tag{A26a}$$

$$\tau_{23} = C_2 + \frac{\partial p}{\partial x_2}x_3, \tag{A26b}$$

where C_1 and C_2 are constants of integration. Substituting (A26) into (A25) yields

$$\frac{du_1}{dx_3} = C\left(\left(C_1 + \frac{\partial p}{\partial x_1}x_3\right)^2 + \left(C_2 + \frac{\partial p}{\partial x_2}x_3\right)^2\right)\left(C_1 + \frac{\partial p}{\partial x_1}x_3\right) \tag{A27a}$$

$$\frac{du_2}{dx_3} = C\left(\left(C_1 + \frac{\partial p}{\partial x_1}x_3\right)^2 + \left(C_2 + \frac{\partial p}{\partial x_2}x_3\right)^2\right)\left(C_2 + \frac{\partial p}{\partial x_2}x_3\right). \tag{A27b}$$

Non-dimensionalizing (A27) leads to

$$\frac{dU_1}{dX_3} = \alpha\beta_{x_1}\left(\beta_{x_1}^2(C_1 + X_3)^2 + \beta_{x_2}^2(C_2 + X_3)^2\right)(C_1 + X_3) \tag{A28a}$$

$$\frac{dU_2}{dX_3} = \alpha\beta_{x_2}\left(\beta_{x_1}^2(C_1 + X_3)^2 + \beta_{x_2}^2(C_2 + X_3)^2\right)(C_2 + X_3), \tag{A28b}$$

where C_1 and C_2 are now dimensionless constants of integration and

$$\alpha = \frac{CH^4}{u_o}\mid \nabla p \mid^3 \tag{A29}$$

$$\beta_{x_1} = \frac{\partial p}{\partial x_1}\frac{1}{\mid \nabla p \mid} \tag{A30}$$

$$\beta_{x_2} = \frac{\partial p}{\partial x_2}\frac{1}{\mid \nabla p \mid} \tag{A31}$$

$$\mid \nabla p \mid^2 = \left(\frac{\partial p}{\partial x_1}\right)^2 + \left(\frac{\partial p}{\partial x_2}\right)^2 \tag{A32}$$

$$\theta = \tan^{-1}\left(\frac{\beta_{x_2}}{\beta_{x_1}}\right). \tag{A33}$$

Note that α and θ are free dimensionless parameters that control the magnitude and orientation of the dimensionless horizontal pressure gradient, respectively. Next, we integrate (A28) with respect to X_3 and obtain

$$U_1(X_3) = \frac{\alpha\beta_{x_1}^3}{4}(C_1 + X_3)^4 + \alpha\beta_{x_1}\beta_{x_2}^2\left(C_1 C_2^2 X_3 + C_1 C_2 X_3^2 + \right.$$
$$\left. +\frac{C_1 X_3^3}{3} + \frac{C_2^2 X_3^2}{2} + \frac{2C_2 X_3^3}{3} + \frac{X_3^4}{4}\right) + A \tag{A34a}$$

$$U_2(X_3) = \frac{\alpha\beta_{x_2}^3}{4}(C_2 + X_3)^4 + \alpha\beta_{x_1}^2\beta_{x_2}\left(C_1^2 C_2 X_3 + C_1 C_2 X_3^2 \right.$$
$$\left. +\frac{C_2 X_3^3}{3} + \frac{C_1^2 X_3^2}{2} + \frac{2C_1 X_3^3}{3} + \frac{X_3^4}{4}\right) + B, \tag{A34b}$$

where A and B are constants of integration. Then, we apply (3) to determine the values of the constants A, B, C_1 and C_2

$$A = 1 - \frac{\alpha\beta_{x_1}^3 C_1^4}{4} \tag{A35a}$$

$$B = -\frac{\alpha\beta_{x_2}^3 C_2^4}{4} \tag{A35b}$$

$$0 = \frac{\alpha\beta_{x_1}^3}{4}(C_1 - 1)^4 + \alpha\beta_{x_1}\beta_{x_2}^2\left(-C_1 C_2^{*2} + C_1 C_2^* - \frac{C_1}{3} + \frac{C_2^2}{2}\right.$$
$$\left.-\frac{2C_2}{3} + \frac{1}{4}\right) + 1 - \frac{\alpha\beta_{x_1}^3 C_1^4}{4} \tag{A35c}$$

$$0 = \frac{P\beta_{x_2}^3}{4}(C_2 - 1)^4 + \alpha\beta_{x_1}^2\beta_{x_2}\left(-C_1^2 C_2 + C_1 C_2 - \frac{C_2}{3} + \frac{C_1^2}{2}\right.$$
$$\left.-\frac{2C_1}{3} + \frac{1}{4}\right) - \frac{\alpha\beta_{x_1}^3 C_1^4}{4}. \tag{A35d}$$

Note that expressions (A35) need to be evaluated numerically. As with the Newtonian case, we differentiate (A34) with respect to X_3 to find an expression that describes the strain rate orientation with depth.